

# ADVANCED MATERIALS

## MEMBRANES

An optical image of a 3D multifunctional integumentary membrane integrated on a Langendorff-perfused rabbit heart is shown. The inset shows an epicardial electrogram recorded using integrated fractal electrodes with PEDOT:PSS coatings, as described by J. A. Rogers and co-workers on page 1731.

# Materials and Fractal Designs for 3D Multifunctional Integumentary Membranes with Capabilities in Cardiac Electrotherapy

Lizhi Xu, Sarah R. Gutbrod, Yinji Ma, Artin Petrossians, Yuhao Liu, R. Chad Webb, Jonathan A. Fan, Zijian Yang, Renxiao Xu, John J. Whalen III, James D. Weiland, Yonggang Huang, Igor R. Efimov, and John A. Rogers\*

Cardiac electrotherapy involves application of electrical potentials or currents to treat arrhythmias. Operational modes range from use of electrical pulses to initiate synchronous beating, known as pacing, strong electrical shocks to reset fibrillatory conduction, known as defibrillation, and radio frequency (RF) electric currents to ablate cardiac tissue to disrupt abnormal focal sources or circuits of propagation, known as cardiac ablation therapy. Such electrotherapies can be delivered using intravenous leads or catheters placed directly on the cardiac tissue, sub-cutaneous leads implanted under the skin, or electrode patches externally mounted on the skin. These systems play critically important roles as clinical delivery paths for the

therapeutic current. Physical constraints, however, limit the nature of the interfaces between the cardiac structures and the electrodes. A trade-off exists between spatial control of the electrode location with respect to the local anatomy and large simultaneous coverage of the tissue. An RF catheter provides precise access to anatomical regions but can only make a single point of contact and burn a small mass of tissue in a single step. Defibrillation vectors simultaneously excite a large mass of tissue but with limited flexibility in their position with respect to the anatomy. No existing clinical method can provide simultaneous electrotherapy with spatiotemporal mapping of physiological parameters for feedback control. One consequence is that defibrillation strategies have remained relatively stagnant in terms of versatility in the way in which energy is delivered. The high voltage shocks that are used in conventional procedures can be extremely painful and they limit the battery life of implantable systems.<sup>[1]</sup> A promising direction for advanced low energy cardiac electrotherapy couples feedback-controlled, targeted defibrillation techniques with greatly reduced voltage and energy requirements.<sup>[2–5]</sup> Multifunctional, conformal platforms of electrodes that can integrate over large areas of cardiac structures enable unusual schemes toward this goal, otherwise inhibited by traditional implantable lead-based delivery paths.

Emerging classes of materials and mechanics concepts in the field of stretchable electronics create new opportunities for integrating high performance electronics with the human body, its organs and various tissues.<sup>[6–12]</sup> Recently described devices, referred to as 3D multifunctional integumentary membranes (3D-MIM), provide conformal electronic platforms that interface with the full 3D geometry of the epicardium.<sup>[13]</sup> Here, 3D imaging and printing techniques enable organ-specific geometric designs in the supporting membranes. High performance electronic materials, interconnect structures, and sensors mount on this platform to yield various spatio-temporal mapping and stimulation capabilities. The results presented in the following expand on these concepts to demonstrate 3D-MIM devices configured for cardiac electrotherapy. Here, ideas in fractal geometry yield compliant, large area low impedance electrodes for electrical stimulation in designs that do not compromise the physical stretchability or the low effective modulus of the overall system. Advanced electrode materials, including nanotextured platinum–iridium (Pt–Ir) alloys and poly(3,4-ethylenedioxythiophene):poly(styrene sulfonate) (PEDOT:PSS), integrate naturally to enable low impedance interfaces that are well suited both for delivering electrical pulses and for sensing intrinsic electrophysiology.

Dr. L. Xu, Y. Liu, R. C. Webb, Z. Yang  
Department of Materials Science and Engineering and  
Frederick Seitz Materials Research Laboratory  
University of Illinois at Urbana-Champaign  
1304 W. Green St., Urbana, IL 61801, USA



S. R. Gutbrod, Prof. I. R. Efimov  
Department of Biomedical Engineering  
Washington University in Saint Louis  
360 Whitaker Hall, 1 Brookings Dr., Saint Louis, MO 63130, USA

Dr. Y. Ma  
Center for Mechanics and Materials  
Tsinghua University  
Beijing 100084, China

Dr. Y. Ma, R. Xu, Prof. Y. Huang  
Department of Civil and Environmental Engineering  
Department of Mechanical Engineering  
Center for Engineering and Health and Skin Disease Research Center  
Northwestern University  
2145 Sheridan Road, Evanston, IL 60208, USA

Dr. A. Petrossians, Dr. J. J. Whalen III, Prof. J. D. Weiland  
Department of Chemical Engineering and Materials Science  
Department of Ophthalmology  
Department of Biomedical Engineering  
University of Southern California  
Los Angeles, CA 90033, USA

Prof. J. A. Fan  
Department of Electrical Engineering  
Stanford University  
307 Spilker Building, 348 Via Pueblo, Stanford, CA 94305–4088, USA

Prof. J. A. Rogers  
Department of Materials Science and Engineering  
Beckman Institute for Advanced Science and Technology and  
Frederick Seitz Materials Research Laboratory  
University of Illinois at Urbana-Champaign  
1304 W. Green St., Urbana, IL 61801, USA  
E-mail: jrogers@illinois.edu

DOI: 10.1002/adma.201405017

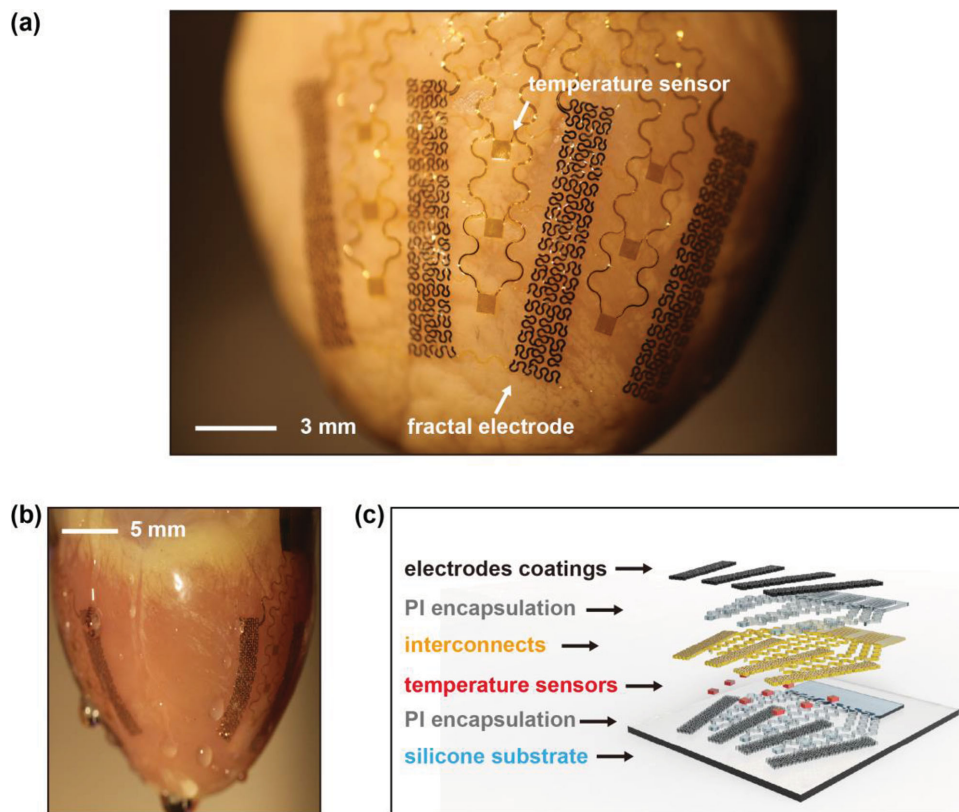


**Figure 1.** a) Image of a representative device integrated on a Langendorff-perfused rabbit heart. The white arrows highlight functional components. b) Side view image. c) Schematic exploded view illustration of device structures and functional components.

These constructs, particularly when co-integrated with high performance sensors, yield versatile platforms for cardiac electrotherapy, of relevance to both basic research and clinical applications. Experiments on in vitro Langendorff-perfused rabbit hearts demonstrate the operational capabilities of these systems.

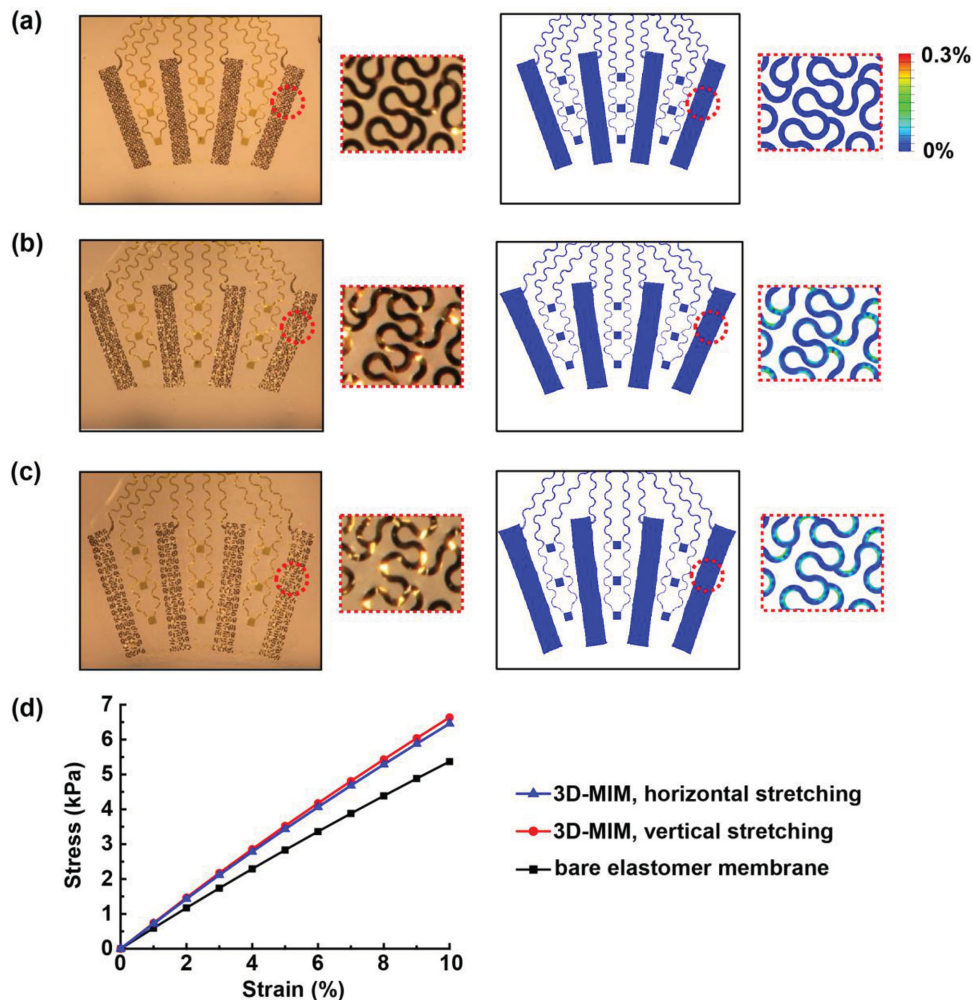
The core component of the devices reported here is an array of 8 electrodes distributed around the circumference of the heart (Figure 1a,b). These electrodes provide direct interfaces for delivering spatially and temporally programmed electrical stimulation across a large area of the epicardium. A conformal interface follows from the use of a thin, low modulus, 3D membrane that is formed in a geometry that matches the epicardial surface, using techniques reported recently.<sup>[13]</sup> Briefly, 3D imaging and printing techniques render solid models that correspond to the targeted heart. Components for sensors and actuators, prefabricated in ultrathin configurations and interconnected by filamentary serpentine traces on planar substrates, are then transferred and temporarily mounted onto the surface of the 3D model. A thin, soft silicone elastomer ( $\approx 100 \mu\text{m}$ ) cast and cured on this model serves as the 3D substrate for the active components. A flexible cable (Elform) provides electrical connection to external hardware. Electrochemical approaches can be employed after these fabrication steps to modify the surfaces of the electrodes. Figure 1a,b shows a representative device integrated on a Langendorff-perfused rabbit heart. The active and passive components maintain conformal contact with the cardiac tissue across the entire surface of the epicardium (Figure 1b), throughout the natural cycles of beating.

Figure 1c shows the materials components and illustrates a general integration scheme for functional elements of the device. A silicone elastomer (Ecoflex, Smooth-on) with low elastic modulus ( $\approx 60 \text{ kPa}$ ) serves as the mechanical support for the active components. This non-conductive substrate may also help contain the electrotherapy to within the boundaries of the membrane, which could potentially reduce pain associated with high-voltage shocks and improve the efficiency of defibrillation. A co-integrated array of resistive temperature sensors based on Au traces ( $15 \mu\text{m}$  in width and  $70 \text{ nm}$  in thickness) yields information useful for monitoring ablation therapy. Depending on application requirements, various microfabricated sensors and actuators including high performance semiconductor devices can be included as well, integrated using the methods of transfer printing.<sup>[13]</sup> Thin layers of Au ( $300 \text{ nm}$ ) and Ti ( $5 \text{ nm}$ ) serve as interconnects as well as conductive surfaces for electrode deposition and processing described next. Polyimide (PI) layers ( $1.2 \mu\text{m}$ ) provide electrical insulation. Low-impedance coatings of nanotextured Pt–Ir alloys or PEDOT:PSS can be electrodeposited to yield high quality electrical interfaces.

Fractal design concepts for the electrodes enable large area coverage and high filling fraction for electrically active surfaces, suitable for generating electric fields across cardiac tissue, but without compromising stretchability and compliance.<sup>[14]</sup> Here, the pattern for each electrode exploits a 2nd order iteration of the Greek cross fractal motif, with serpentine traces that fill a rectangular area with dimension of  $14.5 \text{ mm} \times 2.5 \text{ mm}$ . Serpentine with widths of  $100 \mu\text{m}$  result in a filling fraction of 44%, thereby

providing  $14 \text{ mm}^2$  of geometrical surface area for each electrode. By comparison to previously reported 3D-MIM electrodes, the present configuration increases the surface area by a factor of  $\approx 14$  and increases the overall dimension (defined by the area of the perimeter of the electrode structure) by a factor of  $\approx 36$ . The Greek cross involves a high degree of geometrical connectivity, to reduce the electrical resistance and provide a high degree of tolerance to defects. An additional benefit of this design relates to the non-uniform distribution of current on the electrode surfaces, where additional charge distributes at the electrode edges. The unique layouts of these fractal geometries increase the ratio of the electrode-insulation edge length to the geometric surface area of the electrode, when compared to a conventional electrode of equivalent geometric area. It is well understood that current at an electrochemical electrode interface is preferentially distributed at the electrode-insulation edges.<sup>[15–17]</sup> This observation suggests that a fractal electrode of equivalent geometric area to a conventional electrode design should transfer current more efficiently from the electrode to the tissue. These improvements are particularly beneficial to the development of low power systems.

The mechanics of these structures are also critically important. Finite element analysis (FEA) illuminates the response of the fractal electrodes to applied strains, throughout a range associated with 3D integration and operation on the surface of a beating heart. As shown in Figure S1 in the Supporting Information, the effective modulus of the fractal electrode element is  $\approx 120 \text{ kPa}$ , and it can accommodate 15% stretching in either the vertical or horizontal direction before reaching a regime of plastic deformation. By comparison, the intrinsic modulus and yield strain of the constituent metals are  $\approx 100 \text{ GPa}$  and  $\approx 0.3\%$ , respectively. The overall mechanical behavior of the integrated device must meet two requirements: i) sufficient stretchability for the device to allow deformations associated with contraction and relaxing of the heart muscle, and ii) minimal force exerted by the device on structures of the epicardial surface. Finite element analysis (FEA) in combination with uniaxial and biaxial stretching experiments reveals the geometry change, strain distribution, and effective modulus of the device, as parameters that determine the ability to meet these two requirements. **Figure 2a–c** displays the device



**Figure 2.** a–c) Optical images (left) and FEA results of the distribution of maximum principal strain (right) of a representative device a) in the undeformed state, b) with 20% uniaxial stretching in the horizontal direction, and c) with 15% biaxial stretching. The insets show magnified views of the fractal electrode. d) FEA results of the stress–strain relation of the elastomer membrane and the 3D-MIM.

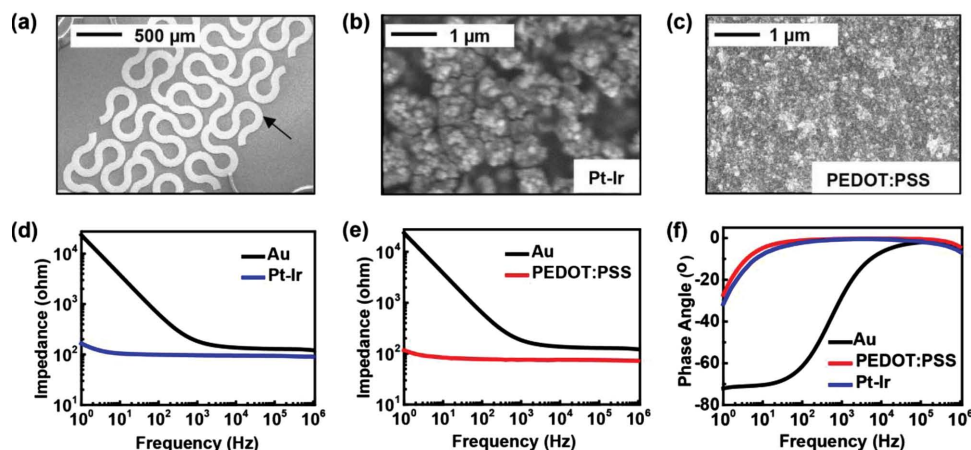


**Figure 3.** a) SEM image of a fractal electrode. b) SEM image of the surface of a Pt–Ir alloy coating. c) SEM image of the surface of a PEDOT:PSS coating. d) Bode magnitude plot of electrochemical impedance spectroscopy (EIS) data for the Au base electrode and the nano-textured Pt–Ir alloy coated electrode. e) Bode magnitude plot of EIS data for the Au base electrode and the PEDOT:PSS coated electrode. f) Bode phase plot of EIS data for the Au base electrode, the nano-textured Pt–Ir alloy coated electrode and the PEDOT:PSS coated electrode.

geometry and strain distribution in the undeformed state, with 20% uniaxial stretching and with 15% biaxial stretching, respectively. The uniaxial stretch is in the horizontal direction, corresponding to the atrioventricular plane, which makes the largest contribution to total heart volume change associated with diastole/systole cardiac cycles.<sup>[18]</sup> As shown in Figure 2b, the resulting strain is accommodated by deformation of the soft elastomer substrate and buckling of the serpentine features. The maximum principal strain obtained by FEA, shown in Figure 2b (also Figure S2, Supporting Information), is less than 0.3%, which is within the elastic regime for the metal and is far less than the fracture strain for all constituent materials (Ti, Au, Pt–Ir, polymer). Figure 2c and Figure S3 in the Supporting Information, display similar characteristics for 15% biaxial stretching. These results suggest that the device can withstand the mounting process as well as the contraction and relaxation of the heart muscles, which result in 10–15% of tensile deformation.<sup>[13]</sup>

The second requirement demands minimal constraint on the heart, which is equivalent to minimizing the effective modulus of the device to reduce the average pressure that it exerts on the heart.<sup>[13,19]</sup> Figure 2d shows the linear relationship between the stress and strain for the elastomer membrane and the 3D-MIM (i.e., membrane with interconnected devices). The effective modulus (slope in Figure 2d) is dominated by the silicone membrane ( $\approx 150 \mu\text{m}$  in thickness, with modulus  $\approx 60 \text{ kPa}$ ). The modulus for the 3D-MIM is only slightly larger, i.e., 71 kPa (horizontal stretching) and 74 kPa (vertical stretching). The calculated average pressure associated with integration of the device on the heart in its diastolic state (145% of the contracted volume) is  $\approx 273 \text{ Pa}$  (Figure S4, Supporting Information), which is similar to the pericardial pressure under normal physiological states and well below the values associated with pericardial constraint.<sup>[19–21]</sup> These results indicate that the device is unlikely to cause restrictive impact on the intrinsic cardiac cycles, consistent with all of our experimental observations.

Reducing the electrochemical impedance associated with the interface between the electrodes and the cardiac tissue

improves the signal-to-noise ratio (SNR) for recording biopotentials and lowers the power consumption for electrical stimulation.<sup>[17]</sup> Lowering the impedance also enables reductions in electrode size without compromising charge capacity, thereby allowing improved current focusing and reduced probability of pain or other side effects caused by aberrant current, high-voltage, and high-energy electrical shocks. The large area fractal electrodes dramatically reduce the impedance compared to previous designs, as shown in Figure S6, Supporting Information. Pt–Ir alloys with nanoscale surface textures and PEDOT:PSS films represent two attractive options that are compatible with the platforms and fabrication procedures reported here. The former exploits recently reported electrochemical deposition methods<sup>[22]</sup> to yield electrodes with enhanced mechanical and electrical properties compared to more conventional alternatives such as Pt, Pt black, or standard Pt–Ir alloys. We implemented this technology as a surface modification to the previously described fractal electrodes. The morphology of the electrochemically modified electrodes appears in high-resolution scanning electron microscope (SEM) (Hitachi S4800) images in Figure 3a,b. Characterization by electrochemical impedance spectroscopy (EIS) involves measurements in phosphate buffered saline, using a commercial potentiostat (Gamry Reference 600) with integrated frequency analyzer (EIS 300). EIS data from fractal electrodes with and without the nanotextured Pt–Ir coating appear in Figure 3d,f in the form of Bode plots. Compared to the base Au electrode, the nanotextured Pt–Ir reduces the electrochemical impedance,  $|Z|$ , by  $10^1$  at a frequency of 100 Hz. In addition to traditional metals, conducting polymers, such as PEDOT:PSS and polypyrrole (PPy), can be considered.<sup>[23–25]</sup> Such materials exhibit low electrochemical impedance, mechanical flexibility, and good biocompatibility. Electro-polymerization provides a convenient method to form coatings of PEDOT:PSS on Au electrode surfaces. The deposition uses constant voltage mode (1.1 V with respect to Ag/AgCl reference electrode) in an aqueous solution containing 3,4-ethylenedioxythiophene (EDOT) (0.1 wt%) and poly(sodium 4-styrenesulfonate) (PSSNa) (0.2 wt%). The SEM

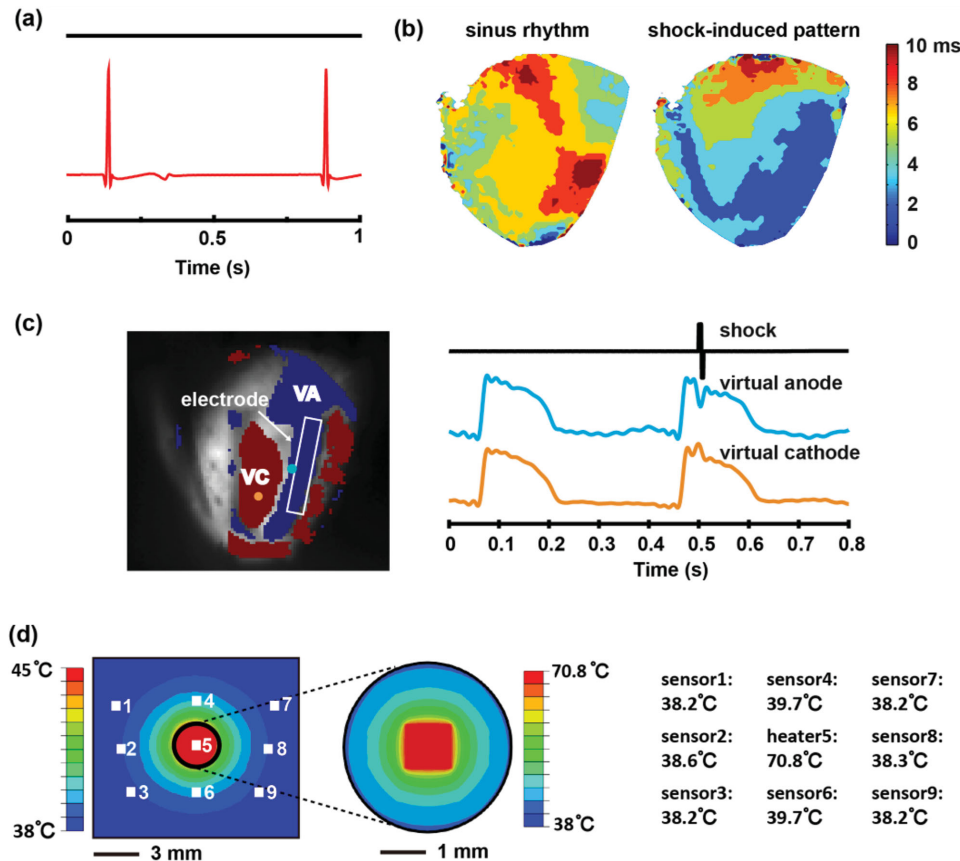


**Figure 4.** a) A representative epicardial electrogram recorded with a PEDOT:PSS electrode. b) Activation maps created from optical signals on one side of the epicardium during a sinus beat (left) and immediately following a 50 V shock (right) from a Langendorff-perfused rabbit heart. c) Virtual electrode pattern and representative traces from the virtual anode and the virtual cathode illustrating the effect of a 50 V shock applied across the heart from the device. The electrode used shown in the field of view is highlighted in white. d) Left: Positions of the temperature sensors/heater (white boxes) and the steady-state temperature distribution on the epicardium obtained by FEA. Right: Steady-state temperature recordings from each of the temperature sensors/heater by experiment.

image and EIS data of the coated electrode appear in Figure 3c,e,f. Similar to the nanotextured Pt–Ir alloy coating, the PEDOT:PSS reduces the electrochemical impedance dramatically in the low frequency range (1–1000 Hz), with a impedance magnitude of  $\approx 100 \Omega$  at 100 Hz. Impedances at high frequency for both the bare Au electrodes and the modified electrodes arise mostly from resistance of the solution and the series resistance of the interconnects. These selections for electrode materials are only representative, where the goal is to illustrate the diversity of low impedance electrode materials that can be embodied in 3D-MIM formats for cardiac applications. Many coating materials can be also considered, including Pt, Pt black, and  $\text{IrO}_x$ .<sup>[26–28]</sup> The thin film coatings have minor effects on the mechanics of the devices; controlling their thicknesses can be considered for fine optimization.

Animal experiments on Langendorff-perfused rabbit hearts demonstrate the multifunctional operation of the devices. Epicardial electrograms recorded with a PEDOT:PSS electrode (Figure 4a) display clear signals expected from the QRS and T features of the waveforms. To simulate defibrillation therapy, 50 V electrical shocks were applied through each pair of electrodes (with Pt coated surfaces) integrated on the epicardium

to form vectors that traverse the ventricles. Optically imaged action potentials from the epicardium demonstrate an immediate tissue response to the applied electrotherapy. The video in the Supporting Information, shows the potential during a sinus beat followed by a shock induced beat to illustrate effective capture with a single vector. Figure 4b compares the activation pattern of the sinus beat with the shock-induced activation. The varying spatial response in activation time confirms effective capture. The virtual electrode pattern (VEP) induced by high voltage shocks is an important feature that determines the mechanism of successful electrotherapy.<sup>[29]</sup> Figure 4c illustrates this characteristic pattern following a 50 V shock delivered from the electrode highlighted in white. This simple demonstration establishes feasibility of creating stretchable thin film electrodes that can carry high voltage and large current shocks to the cardiac tissue. Repeated high-voltage shocks have the potential to induce corrosive degradation of the thin metal layers used in these electrodes. Further investigation will be necessary for chronic operation of this type of high-voltage electrotherapy.

A co-integrated array of 9 temperature sensors/heaters interfaces with the epicardial surface (Figure 1a) can be useful for monitoring ablation procedures. As an example, the center

resistor in the array can act as a Joule heating element to elevate the surface temperature to 70.8 °C from a baseline of 38 °C, as a mimic of point contact ablation. The surrounding resistors then serve as sensors to measure the spatial distribution of the resulting rise in temperature. The experiments indeed show local temperature increases around the heater (Figure 4d), in agreement with the temperature field obtained by FEA (see the Supplementary Note and Table S1 in the Supporting Information). The increase of temperature decays rapidly with distance from the heater. The temperature change is  $\approx 1.7$  °C at locations 4 mm from the heater, and only  $\approx 0.2$  °C at 8.7 mm. This capability for characterizing spatial distributions of temperature can be helpful for guiding precise delivery of cardiac ablation therapy.

In summary, advanced designs and materials approaches provide capabilities for cardiac electrotherapy in an advanced 3D-MIM platform. Concepts in fractal geometry allow large area, conformal electrodes suitable for delivering cardiac electrical stimulation, and for sensing cardiac electrical activity. Surface coating materials improve the electrochemical characteristics of the electrodes, in ways that are naturally compatible with the platform and its fabrication. Integrated arrays of sensors can be used to precisely monitor the electrotherapy and other forms of intervention. Animal experiments demonstrate the multifunctional operation of the devices. These results suggest routes for developing advanced tools with utility in both fundamental research and clinical application of cardiac electrotherapy.

## Experimental Section

**Processing for Electrode Coatings:** i) Pt–Ir alloy with nanoscale surface textures: Electrochemical deposition of Pt–Ir used a mixed plating bath of ammonium hexachloroplatinate and hexachloroirridate. The details appear elsewhere.<sup>[22]</sup> Immersing bare electrode surfaces in the plating bath followed by application of a controlled electrochemical potential (Gamry Reference 600 in a 3-electrode system) caused chemical reduction of metal ions in solution to metal alloys on the electrode surfaces. The deposition conditions define the morphology and composition of the resulting coatings. ii) PEDOT:PSS coatings: 0.2 g of EDOT (Sigma–Aldrich) added to 200 mL deionized water, stirred overnight for complete dissolution, followed by 0.4 g of PSSNa (Sigma–Aldrich) yielded the solution for electro-polymerization. A potentiostat (Gamry Reference 600) controlled the electro-polymerization processes in a 3-electrode configuration. Immersing the selected electrodes on the 3D-MIM into the solution and applying a constant voltage (1.1 V to Ag/AgCl reference electrode) for 10 min, formed the desired coating, as evidence by a change in the color of the electrode surface from gold to dark blue/black. For values above a certain level, the thicknesses of the coatings have little effect on the electrochemical impedance.

**Animal Experiments:** The animal study was approved by the Institutional Animal Care and Use Committee of Washington University School of Medicine. The heart was obtained from a New Zealand white rabbit, anesthetized with an intravenous injection of 80 mg kg<sup>-1</sup> of sodium pentobarbital and 400 USP units kg<sup>-1</sup> of heparin before the heart was surgically explanted. The heart was then transferred to a tissue bath that maintained the temperature ( $37 \pm 1$  °C) and pH ( $7.4 \pm 0.05$ ) to mimic physiological conditions. The heart was retrogradely perfused under a constant pressure of 60–80 mm Hg with oxygenated Tyrode's solution (95% O<sub>2</sub>/5% CO<sub>2</sub>, NaCl  $128.2 \times 10^{-3}$ , CaCl  $1.3 \times 10^{-3}$ , KCl  $4.7 \times 10^{-3}$ , MgCl<sub>2</sub>  $1.05 \times 10^{-3}$ , NaH<sub>2</sub>PO<sub>4</sub>  $1.19 \times 10^{-3}$ , NaHCO<sub>3</sub>  $20.0 \times 10^{-3}$ , glucose  $11.1 \times 10^{-3}$  M). The heart was mechanically uncoupled

with  $15 \times 10^{-6}$  M Blebbistatin (Cayman Chemical, Ann Arbor, MI) and perfused with a bolus injection of di-4 ANEPPS (Life Technologies, Grand Island, NY, USA). The 3D-MIM was placed over the heart, positioned with 4 electrodes across the anterior surface and 4 electrodes on the posterior surface. The electrodes were connected in pairs to a custom defibrillator (Cardialen, Inc, St Louis, MO, USA) that delivered 50–100 V biphasic truncated exponential pulses (phase 1 duration 6 ms, phase 2 duration 4 ms, phase 2 voltage was half the peak amplitude and opposite polarity voltage of phase 1). Optical action potentials were recorded before, during, and after delivery of the shock from two CMOS cameras (SciMedia Ltd, Costa Mesa, Ca, USA) with 520 nm excitation light through a long pass emission filter with a 650 nm cutoff. The data were then processed with custom Matlab software.<sup>[30]</sup> The VEP was determined by evaluating the sign of the optical action potential derivative from the time of the shock until 10 ms past the shock.

## Supporting Information

Supporting Information is available from the Wiley Online Library or from the author.

## Acknowledgements

This material is based upon work supported by the NIH Grant Nos. R01 HL115415, R01 HL114395, and R21 HL112278, and through the Frederick Seitz Materials Research Laboratory and Center for Microanalysis of Materials at the University of Illinois at Urbana-Champaign. L.X. acknowledges support from China Scholarship Council. R.C.W. acknowledges support from the National Science Foundation under Grant No. DGE-1144245.

Received: November 2, 2014

Revised: November 26, 2014

Published online: January 12, 2015

- [1] I. Flemme, N. Edvardsson, H. Hinic, B. M. Jinhage, M. Dalman, B. Fridlund, *Heart Lung* **2005**, *34*, 386.
- [2] W. W. Li, C. M. Ripplinger, Q. Lou, I. R. Efimov, *Heart Rhythm* **2009**, *6*, 1020.
- [3] A. H. Janardhan, W. W. Li, V. V. Fedorov, M. Yeung, M. J. Wallendorf, R. B. Schuessler, I. R. Efimov, *J. Am. Coll. Cardiol.* **2012**, *60*, 2393.
- [4] S. Luther, F. H. Fenton, B. G. Kornreich, A. Squires, P. Bittihn, D. Hornung, M. Zabel, J. Flanders, A. Gladuli, L. Campoy, E. M. Cherry, G. Luther, G. Hasenfuss, V. I. Krinsky, A. Purnir, R. F. Gilmour, E. Bodenschatz, *Nature* **2011**, *475*, 235.
- [5] R. A. S. Cooper, W. M. Smith, R. E. Ideker, *Circulation* **1997**, *96*, 2693.
- [6] D.-H. Kim, N. Lu, R. Ma, Y.-S. Kim, R.-H. Kim, S. Wang, J. Wu, S. M. Won, H. Tao, A. Islam, K. J. Yu, T.-I. Kim, R. Chowdhury, M. Ying, L. Xu, M. Li, H.-J. Chung, H. Keum, M. McCormick, P. Liu, Y.-W. Zhang, F. G. Omenetto, Y. Huang, T. Coleman, J. A. Rogers, *Science* **2011**, *333*, 838.
- [7] M. Ying, A. P. Bonifas, N. S. Lu, Y. W. Su, R. Li, H. Y. Cheng, A. Ameen, Y. G. Huang, J. A. Rogers, *Nanotechnology* **2012**, *23*, 344004.
- [8] D. H. Kim, J. Viventi, J. J. Amsden, J. L. Xiao, L. Vigeland, Y. S. Kim, J. A. Blanco, B. Panilaitis, E. S. Frechette, D. Contreras, D. L. Kaplan, F. G. Omenetto, Y. G. Huang, K. C. Hwang, M. R. Zakin, B. Litt, J. A. Rogers, *Nat. Mater.* **2010**, *9*, 511.
- [9] D.-H. Kim, N. Lu, R. Ghaffari, Y.-S. Kim, S. P. Lee, L. Xu, J. Wu, R.-H. Kim, J. Song, Z. Liu, *Nat. Mater.* **2011**, *10*, 316.

- [10] H. F. Yao, A. J. Shum, M. Cowan, I. Lahdesmaki, B. A. Parviz, *Biosens. Bioelectron.* **2011**, *26*, 3290.
- [11] M. Kaltenbrunner, T. Sekitani, J. Reeder, T. Yokota, K. Kuribara, T. Tokuhara, M. Drack, R. Schwodiauer, I. Graz, S. Bauer-Gogonea, S. Bauer, T. Someya, *Nature* **2013**, *499*, 458.
- [12] D. J. Lipomi, M. Vosgueritchian, B. C. K. Tee, S. L. Hellstrom, J. A. Lee, C. H. Fox, Z. N. Bao, *Nat. Nanotechnol.* **2011**, *6*, 788.
- [13] L. Z. Xu, S. R. Gutbrod, A. P. Bonifas, Y. W. Su, M. S. Sulkin, N. S. Lu, H. J. Chung, K. I. Jang, Z. J. Liu, M. Ying, C. Lu, R. C. Webb, J. S. Kim, J. I. Laughner, H. Y. Cheng, Y. H. Liu, A. Ameen, J. W. Jeong, G. T. Kim, Y. G. Huang, I. R. Efimov, J. A. Rogers, *Nat. Commun.* **2014**, *5*, 3329.
- [14] J. A. Fan, W. H. Yeo, Y. W. Su, Y. Hattori, W. Lee, S. Y. Jung, Y. H. Zhang, Z. J. Liu, H. Y. Cheng, L. Falgout, M. Bajema, T. Coleman, D. Gregoire, R. J. Larsen, Y. G. Huang, J. A. Rogers, *Nat. Commun.* **2014**, *5*, 3266.
- [15] A. K. Ahuja, M. R. Behrend, J. J. Whalen, M. S. Humayun, J. D. Weiland, *IEEE Trans. Biomed. Eng.* **2008**, *55*, 1457.
- [16] J. Newman, *J. Electrochem. Soc.* **1966**, *113*, 501.
- [17] S. F. Cogan, *Annu. Rev. Biomed. Eng.* **2008**, *10*, 275.
- [18] M. Carlsson, P. Cain, C. Holmqvist, F. Stahlberg, S. Lundback, H. Arheden, *Am. J. Physiol. Heart. Circ. Physiol.* **2004**, *287*, H243.
- [19] R. Shabetai, *Heart* **2004**, *90*, 255.
- [20] J. P. Holt, E. A. Rhode, H. Kines, *Circ. Res.* **1960**, *8*, 1171.
- [21] E. W. Hancock, *Circulation* **1971**, *43*, 183.
- [22] A. Petrossians, J. J. Whalen, J. D. Weiland, F. Mansfeld, *J. Electrochem. Soc.* **2011**, *158*, D269.
- [23] K. A. Ludwig, N. B. Langhals, M. D. Joseph, S. M. Richardson-Burns, J. L. Hendricks, D. R. Kipke, *J. Neural Eng.* **2011**, *8*, 014001.
- [24] L. Guo, M. M. Ma, N. Zhang, R. Langer, D. G. Anderson, *Adv. Mater.* **2014**, *26*, 1427.
- [25] R. A. Green, N. H. Lovell, G. G. Wallace, L. A. Poole-Warren, *Biomaterials* **2008**, *29*, 3393.
- [26] C. R. K. Rao, D. C. Trivedi, *Coord. Chem. Rev.* **2005**, *249*, 613.
- [27] R. D. Meyer, S. E. Cogan, T. H. Nguyen, R. D. Rauh, *IEEE Trans. Neural Syst. Rehabil. Eng.* **2001**, *9*, 2.
- [28] A. Feltham, M. Spiro, *Chem. Rev.* **1971**, *71*, 177.
- [29] I. Efimov, C. M. Ripplinger, *Heart Rhythm* **2006**, *3*, 1100.
- [30] J. I. Laughner, F. S. Ng, M. S. Sulkin, R. M. Arthur, I. R. Efimov, *Am. J. Physiol. Heart. Circ. Physiol.* **2012**, *303*, H753.